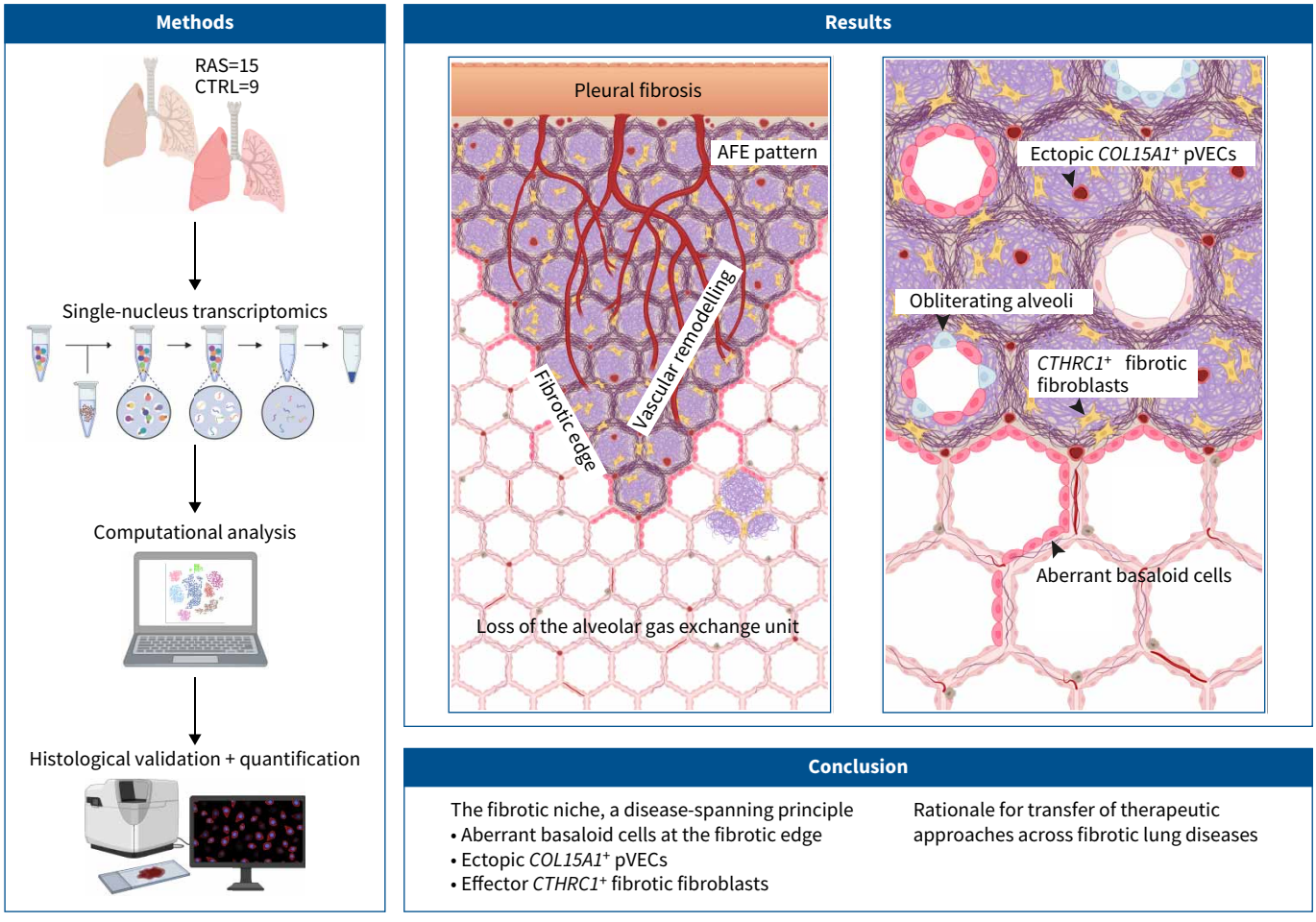
Aberrant and ectopic cell populations in restrictive allograft syndrome after lung transplantation

Lena M. Leiber, Leonard Christian, Lavinia Neubert, Jannik Ruwisch, Hande Yilmaz, Edith K.J. Schwarz, Linus T. Langer, Jan C. Kamp, Mark Greer, Bernd Haermeyer, Mark Kühnel, Christopher Werlein, Aurelien Justet, Anke K. Bergmann, Hanne Beeckmans, Matthias Ballmaier, Jawad Salman, Robin Vos, Lars Knudsen, Ulrich Martin, Bart M. Vanaudenaerde, Ali Önder Yildirim, Jens M. Hohlfeld, Fabio Ius, Florian Laenger, Tobias Welte, Christine Falk, Naftali Kaminski, Danny D. Jonigk, Jens Gottlieb and Jonas C. Schupp



GRAPHICAL ABSTRACT Overview of the study. RAS: restrictive allograft syndrome; CTRL: control; AFE: alveolar fibroelastosis; pVEC: peribronchial vascular endothelial cell.

https://doi.org/10.1183/13993003.00537-2025 Eur Respir J 2026; 68: 2500537

Downloaded from https://publications.ersnet.org on October 29, 2026 by guest. Please see licensing information on first page for reuse rights.

Aberrant and ectopic cell populations in restrictive allograft syndrome after lung transplantation

Lena M. Leiber [1,2], Leonard Christian[1,2], Lavinia Neubert[2,3], Jannik Ruwisch [1,2], Hande Yilmaz[1,2], Edith K.J. Schwarz [2,3], Linus T. Langer[1,2], Jan C. Kamp [1,2,3], Mark Greer [1,2], Bernd Haermeyer[4], Mark Kühnel [2,5], Christopher Werlein [2,3], Aurelien Justet [6], Anke K. Bergmann [4], Hanne Beeckmans [7], Matthias Ballmaier [8], Jawad Salman[9], Robin Vos [7], Lars Knudsen [10], Ulrich Martin [2,9,11], Bart M. Vanaudenaerde [7], Ali Önder Yildirim [12], Jens M. Hohlfeld [1,2,13], Fabio Ius [2,9], Florian Laenger [5], Tobias Welte [1,2,†], Christine Falk [2,14], Naftali Kaminski [15], Danny D. Jonigk [2,3,5,16], Jens Gottlieb [1,2,16] and Jonas C. Schupp [1,2,13,15,16]

[1]Department of Respiratory Medicine and Infectious Diseases, Hannover Medical School, Hannover, Germany. [2]Biomedical Research in Endstage and Obstructive Lung Disease Hannover, German Center for Lung Research, Hannover, Germany. [3]Institute of Pathology, Hannover Medical School, Hannover, Germany. [4]Institute of Human Genetics, Hannover Medical School, Hannover, Germany. [5]Institute of Pathology, RWTH Aachen, Aachen, Germany. [6]Service de Pneumologie, CHU de Caen, Centre de compétence des maladies pulmonaires rares, ISTCT, UMR6030-CNRS-CEA-Université de Caen, Caen, France. [7]Laboratory of Respiratory Diseases and Thoracic Surgery (BREATHE), KU Leuven, Leuven, Belgium. [8]Central Research Facility Cell Sorting, Hannover Medical School, Hannover, Germany. [9]Clinic for Cardiac, Thoracic, Transplant and Vascular Surgery, Hannover Medical School, Hannover, Germany. [10]Institute for Functional and Applied Anatomy, Hannover Medical School, Hannover, Germany. [11]Leibniz Research Laboratories for Biotechnology and Artificial Organs, Lower Saxony Center for Biomedical Engineering, Implant Research and Development, Hannover, Germany. [12]Institute of Lung Health and Immunity (LHI), Helmholtz Zentrum Muenchen, Institute of Lung Biology and Disease, Munich, Germany. [13]Department of Clinical Airway Research, Fraunhofer Institute for Toxicology and Experimental Medicine (ITEM), Hannover, Germany. [14]Institute of Transplant Immunology, Hannover Medical School, Hannover, Germany. [15]Section of Pulmonary, Critical Care and Sleep Medicine, Yale School of Medicine, New Haven, CT, USA. [16]These authors contributed equally to this work. [†]Died 10 March 2024.

Corresponding author: Jonas C. Schupp (schupp.jonas@mh-hannover.de)

Shareable abstract (@ERSpublications)
snRNA-seq analysis of RAS lungs revealed the general principle of an entity-spanning composition of the usual fibrotic niche consisting of aberrant basaloid cells, ectopic *COL15A1*$^+$ *pVECs*, and CTHRC1$^+$ fibroblasts https://bit.ly/3QdPRmf

Cite this article as: Leiber LM, Christian L, Neubert L, *et al*. Aberrant and ectopic cell populations in restrictive allograft syndrome after lung transplantation. *Eur Respir J* 2026; 68: 2500537 [DOI: 10.1183/13993003.00537-2025].

Copyright ©The authors 2026.

This version is distributed under the terms of the Creative Commons Attribution Non-Commercial Licence 4.0. For commercial reproduction rights and permissions contact permissions@ersnet.org

This article has an editorial commentary: https://doi.org/10.1183/13993003.00991-2026

Abstract

Rationale Restrictive allograft syndrome (RAS) is a major cause of mortality following lung transplantation due to progressive fibrosis of the lung allograft, with no therapeutic options. Knowledge of the cellular and molecular mechanisms driving fibrosis in RAS remains limited.

Objective To characterise the cellular and molecular changes in human RAS lungs through single-nucleus transcriptomic profiling.

Methods Single-nucleus RNA-sequencing (snRNA-seq) was performed in peripheral lung tissues from 15 RAS patients undergoing lung re-transplantation, and from nine healthy control lungs. Findings were validated and extended using histological techniques including immunofluorescence, RNA *in situ* hybridisation, Elastica van Gieson immunohistochemistry, quantitative histological analyses, and micro-computed tomography (CT) scans.

Measurements and main results snRNA-seq analysis of RAS lungs revealed previously undescribed aberrant basaloid cells, ectopic *COL15A1*$^+$ peribronchial vascular endothelial cells (pVECs), and *CTHRC1*$^+$ fibrotic fibroblasts. Histological stains disclosed distinctive distribution patterns: aberrant basaloid cells, primarily localised at the fibrotic edge, together with juxtaposed *CTHRC1*$^+$ fibrotic fibroblasts and ectopic *COL15A1*$^+$ pVECs form the fibrotic niche of alveolar fibroelastosis (AFE). *PRX*$^+$ alveolar microvasculature is partially lost in AFE areas. Micro-CT scans revealed changes from pulmonary

Downloaded from https://publications.ersnet.org on October 29, 2026 by guest. Please see licensing information on first page for reuse rights.

Received: 19 March 2025
Accepted: 13 April 2026

CC BY NC

to systemic perfusion, facilitated by *COL15A1*$^{+}$ pVECs. Lastly, our data reveal potential therapeutic targets in RAS, including integrin αvβ6, activator of transforming growth factor-β.

Conclusion Considering the multifaceted differences of RAS and idiopathic pulmonary fibrosis, we revealed a surprising general principle of an entity-spanning composition of the fibrotic niche by aberrant basaloid cells localised at the fibrotic edge, ectopic *COL15A1*$^{+}$ pVECs and *CTHRC1*$^{+}$ fibrotic fibroblasts. This suggests a flexible, but cellular pathogenesis-guided, transferability of potential therapeutic approaches between progressive fibrotic lung diseases.

Introduction

Chronic lung allograft dysfunction (CLAD) after lung transplantation (LuTx) is an aggressive remodelling process caused by various factors, including allo- and auto-immunity, infection, aspiration and ischaemia. Due to lacking therapeutic options, CLAD remains a major cause of post-lung transplantation morbidity, re-transplantation, and post-lung transplantation mortality. CLAD manifests as restrictive and/or obstructive phenotypes [1–3]. Up to 30% of CLAD patients develop the restrictive phenotype, termed restrictive allograft syndrome (RAS) [2, 4]. RAS is associated with a worse prognosis than the obstructive phenotype, bronchiolitis obliterans syndrome (BOS), with survival rates after diagnosis of 6–18 months *versus* 3–5 years [2, 5–8]. Histologically, RAS lung tissue is characterised by alveolar fibroelastosis (AFE) [6, 9–11], defined by collagenous obliteration of alveoli, and de-epithelisation/elastosis of alveolar walls with only scant inflammation [9, 11]. A peculiar feature of AFE is the sharp transition from fibrosis to alveoli with an inconspicuous architecture, here referred to as the “fibrotic edge” [11].

Much of the current understanding of the pathogenesis and pathognomonic changes in RAS, including risk factors like acute cellular rejection, donor-specific antibodies, and late-onset diffuse alveolar damage, derives from animal models, bronchoalveolar lavage or blood analyses [6, 8, 12–14]. Unpublished single-nucleus RNA-sequencing (snRNA-seq) data suggest that immune mechanisms also contribute to RAS pathogenesis [15]. However, a detailed characterisation of structural cells in RAS lungs remains lacking. In this study, we performed the first single-cell transcriptomic analysis of structural (*i.e.* parenchymal and supporting stromal) lung cells in human RAS lungs using a data-driven approach to elucidate the cellular and gene expression changes underlying the histopathological characteristics of this poorly understood syndrome. We identified by snRNA-seq the previously undescribed presence of aberrant basaloid cells, ectopic *COL15A1*$^{+}$ peribronchial endothelial cells (pVECs) and *CTHRC1*$^{+}$ fibrotic fibroblast populations in RAS. Tissue stains and micro-computed tomography (CT) scans revealed distinctive distribution patterns of these cells, the absence of bronchiolisation in RAS, and a previously undescribed change of perfusion in the RAS lung.

Parts of these data were previously presented as an abstract at the European Respiratory Society Congress 2024 [16].

Material and methods

Detailed experimental methods and stains of control lungs are provided in the supplementary material. We performed snRNA-seq using peripheral lung parenchyma from upper lobes of 15 RAS patients undergoing lung re-transplantation, phenotyped according to current International Society for Heart and Lung Transplantation (ISHLT) criteria, and upper lobe samples from nine control lungs (surgical size adjustment during lung transplantation n=5, histologically tumour-free specimens n=4) (figure 1a, supplementary figure E1, supplementary table E1) [6]. snRNA-seq data were processed with CellRanger and analysed using R and the Seurat package. Transcriptomic data was deposited on Gene Expression Omnibus under the accession number GSE284081. Epithelial, endothelial and stromal cell populations were characterised through iterative clustering followed by differential expression analysis. To focus on structural alterations, immune cells were excluded from this study. Wilcoxon rank sum test with Bonferroni correction of p-values for multiple comparisons established cell type-specific marker genes (supplementary table E2). Epithelial, endothelial and stromal cell subpopulations were validated and localised by immunofluorescent (IF) microscopy, RNA *in situ* hybridisation (RNA-ISH), immunohistochemistry (IHC), and combined Elastica van Gieson (EvG)-IHC stains using formalin-fixed paraffin-embedded samples derived from the same lung explants used for snRNA-seq, enabling direct molecular and histological correlation within individual specimens (n=8 RAS and n=12 control lungs for immunofluorescence; n=5 RAS and n=4 control lungs for RNA-ISH; n=8 RAS and n=4 control lungs for EvG-IHC) (supplementary tables E3 and E4, supplementary figures E2–E23, E27). For quantitative analysis of IF and RNA-ISH images, cell segmentation and machine-learning-based quantification were performed using QuPath (v0.5.1) and the StarDist extension (supplementary figure E24) [18, 19]. Micro-CT scans of two RAS specimens provided further insights into the structural characteristics of RAS. No blinding was performed in this study.

Downloaded from https://publications.ersnet.org on October 29, 2026 by guest. Please see licensing information on first page for reuse rights.

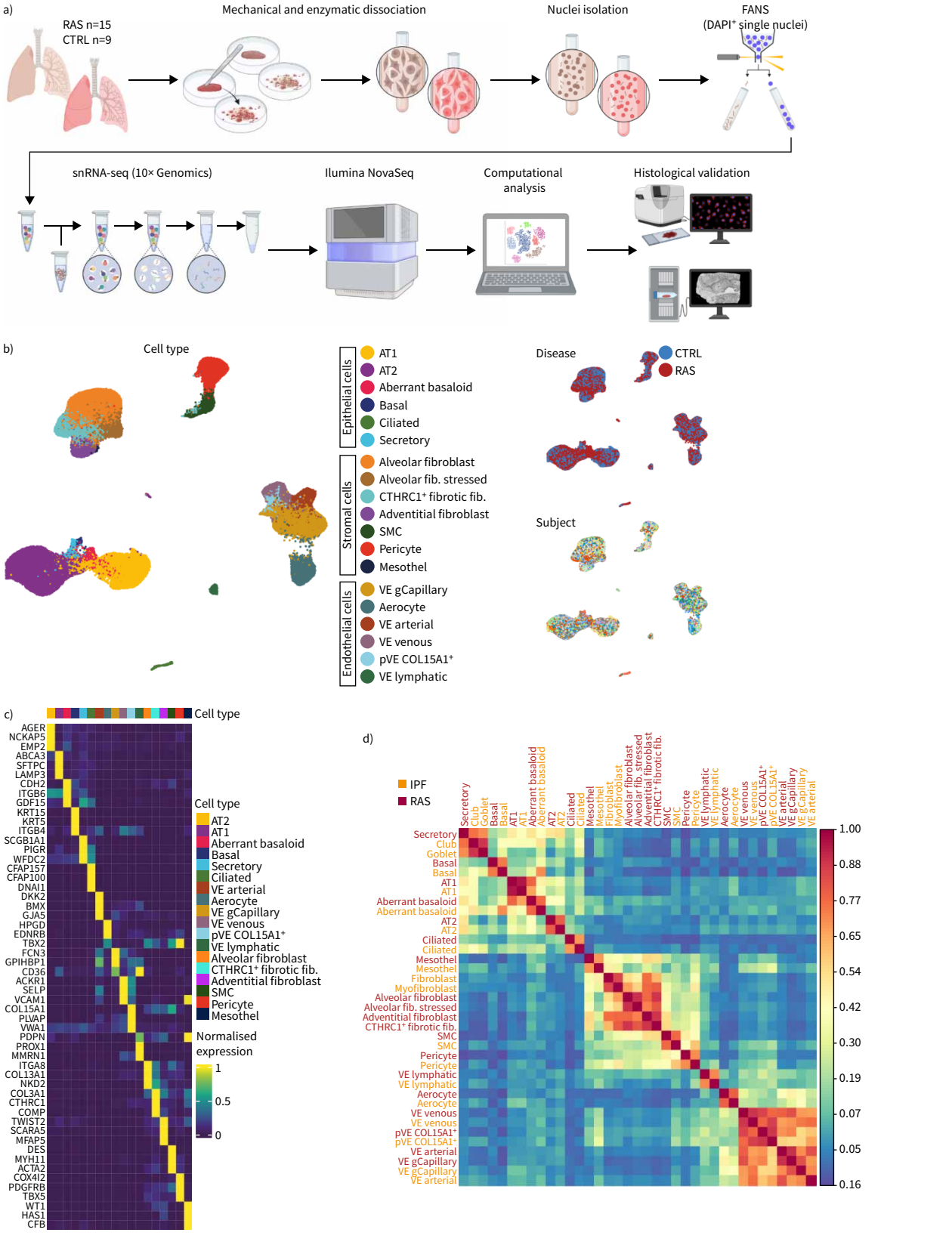


FIGURE 1 Transcriptomic profiling of human restrictive allograft syndrome (RAS) lungs using single-nucleus RNA-sequencing (snRNA-seq). a) Overview of experimental design. Tissue samples of 15 RAS lung explants from patients undergoing lung re-transplantation and from nine donor control (CTRL) lungs were used. The lung tissues were mechanically and enzymatically dissociated, followed by the isolation of nuclei from the dissociated samples. Clean single nuclei suspensions were obtained through flow-activated nuclei sorting (FANS) using

Downloaded from https://publications.ersnet.org on October 29, 2026 by guest. Please see licensing information on first page for reuse rights.

4′,6-diamidino-2-phenylindol (DAPI). For snRNA-seq library preparation, 10× Genomics' Chromium Next GEM technology for multiplexed fixed samples was employed. The prepared libraries were sequenced using the Illumina platform. Subsequent computational analysis was performed to explore and validate the snRNA-seq data. Histological validation and spatial localisation were achieved through immunofluorescence, RNA *in situ* hybridisation, combined Elastica van Gieson-immunohistochemistry stains, and micro-computed tomography scans. b) Uniform manifold approximation and projection (UMAP) representation of 105 952 single nuclei obtained from 15 RAS, and nine control donor lungs. Each dot represents a single nucleus. Nuclei are labelled as one of 19 distinctive cell types in the left UMAP: epithelial cells (alveolar type 1 (AT1), AT2, aberrant basaloid, basal, ciliated and secretory cells), endothelial cells (aerocytes, vascular endothelial (VE) arterial, VE general (g)Capillary, VE lymphatic, VE systemic and VE venous cells), and stromal cells (fibroblasts (alveolar, adventitial, fibrotic and inflamed alveolar), mesothelium (mesothel), pericytes and smooth muscle cells). Additionally, nuclei are labelled by disease status and subject, where each colour depicts a distinct subject. c) Heat map of the average marker gene expression per cell type. Gene expression values are unity-normalised from 0 to 1. d) Correlation matrix of all identified cell populations of this dataset and of analogous parenchymal cell types of the idiopathic pulmonary fibrosis (IPF) atlas [17]. Matrix cells are coloured by Spearman's ρ. Annotation bars (RAS or IPF) denote the origin dataset of each cell population. SMC: smooth muscle cells.

All biological materials and data were collected following written informed consent from the patients and approval from the ethics committee of Hanover Medical School (IRB number 10141_BO_K_2022).

Results

snRNA-seq was applied to 105 952 single nuclei from 15 RAS and nine control specimens (figure 1b). A technical summary, including median unique molecular identifier/genes/reads per nucleus, reads mapped to probe set, and the number of detected genes, is provided in supplementary table E2a. Based on distinct markers, all major lung cell types were identified, as well as aberrant basaloid cells, ectopic *COL15A1*$^{+}$ pVECs and *CTHRC1*$^{+}$ fibrotic fibroblasts, previously discovered in idiopathic pulmonary fibrosis (IPF) [17, 20], but not in RAS (figure 1b–d, supplementary figure E25). Detailed marker gene expressions of all profiled nuclei are provided in supplementary table E2b).

snRNA-seq analysis of the epithelial cell repertoire identified the presence of aberrant basaloid cells in human RAS lungs

40 390 single nuclei (n=24 565 RAS; n=15 825 control), representing 38.1% of all profiled nuclei, were identified as epithelial cells based on distinct marker genes. Major epithelial cell populations of the human lung, including alveolar type 1 (AT1) and type 2 (AT2) cells, basal cells, ciliated cells, and secretory cells were identified in all specimens (figure 2a–d, supplementary table E2c). Additionally, we detected aberrant basaloid cells in all but one of our RAS specimens. This characteristic cell type was first described in 2020 in human IPF lungs, and, to a lesser extent, in COPD lungs [17, 20]. Aberrant basaloid cells express the basal cell markers *KRT17* and *LAMB3* alongside canonical epithelial markers, but lack other established basal cell markers such as *KRT5* and *KRT15*. Furthermore, they express senescence-related genes (*CCND1*, *MDM2* and *GDF15*) and markers of epithelial–mesenchymal transition (EMT) (*CDH2*, *COL1A1*, *VIM* and *FN1*) (figure 2d, supplementary table E2c) [17]. Also, they show the highest expression levels of genes coding for the integrin subunits αvβ6 (*ITGAV*, *ITGB6*), activators of transforming growth factor (TGF)-β, compared to all other cell types in our specimens (figure 2d, supplementary table E2b). Pathway analysis confirmed their unique profile including TGF-β receptor signalling in EMT (supplementary figure E26). We identified 1274 aberrant basaloid cells in RAS matching this unique gene signature, representing a median of 5.4% of the epithelial cell compartment in RAS patients (*versus* controls, unadjusted p<0.0001, Wilcoxon rank-sum test) (figure 2b and c; supplementary table E2h). Correlation analysis with the IPF cell atlas data confirmed the transcriptional concordance of aberrant basaloid cells between RAS and IPF (figure 1d) [17].

Aberrant basaloid cells are localised at the fibrotic edge

We confirmed the presence of aberrant basaloid cells in RAS tissue and investigated their distribution by IF using antibodies against *KRT17*, *TP63*, *CTSE*, *integrin αvβ6* and *COX2*, a distinctive marker combination not overlapping with any other common lung cell type (figure 2d, supplementary table E2b) [17]. Additionally, we included *TP63* for immunofluorescence validation as it is an established and literature-supported characteristic marker gene of aberrant basaloid cells [17, 20–25]. *KRT17*, *TP63* and *integrin αvβ6* served to identify aberrant basaloid epithelial cells, while *CTSE* and *COX2* were interpreted as more broadly expressed epithelial injury marker. All RAS samples exhibited the same characteristic distribution pattern of aberrant basaloid cells: they consistently localise to the margin of the fibrotic edge, lining it almost continuously in a single cell layer. Additionally, aberrant basaloid cells invade the alveolar space in a branching pattern lining fibrotically thickened alveolar septa (figure 3a–c, supplementary figures

Downloaded from https://publications.ersnet.org on October 29, 2026 by guest. Please see licensing information on first page for reuse rights.

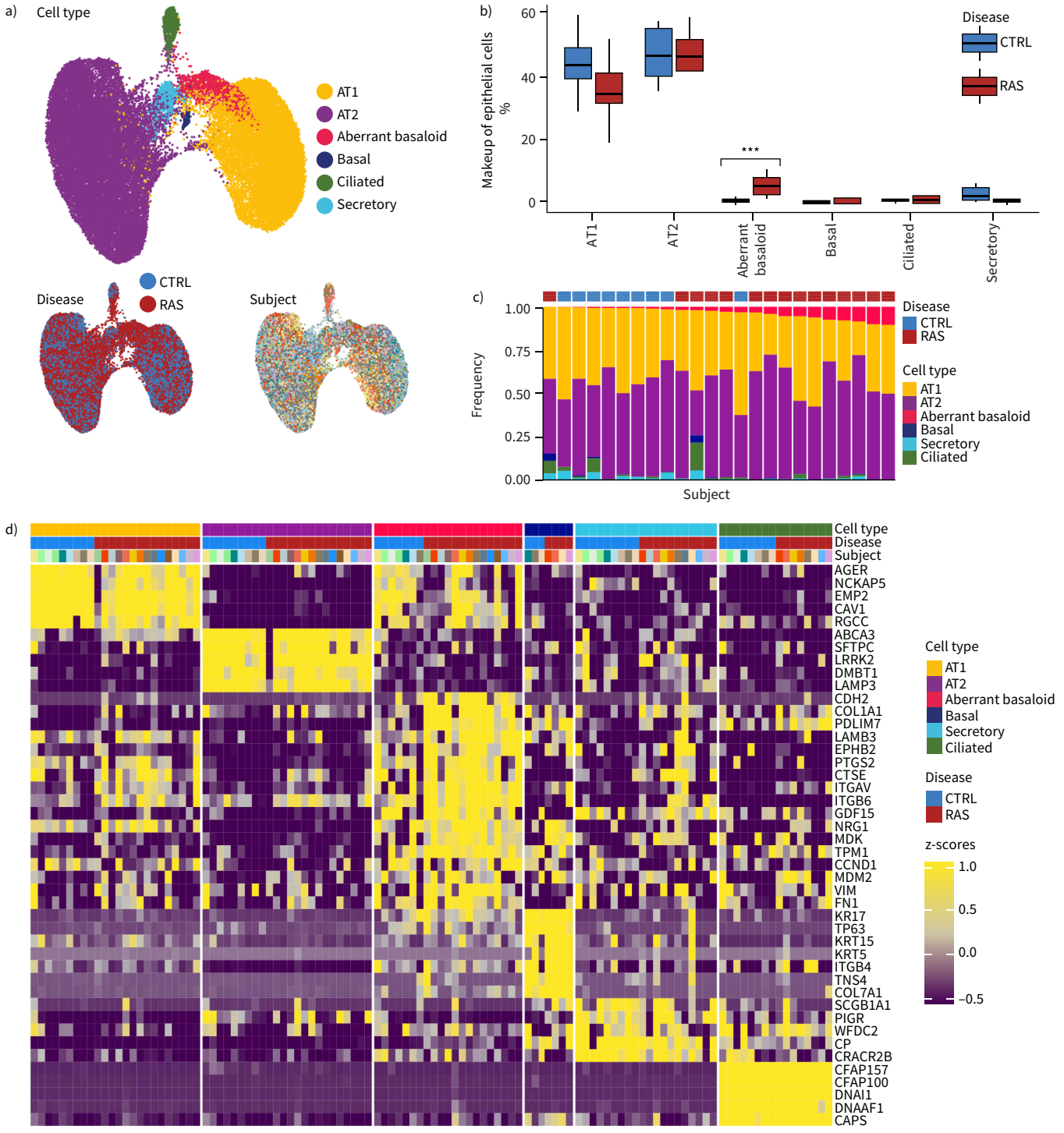


FIGURE 2 Single-nucleus RNA-sequencing (snRNA-seq) analysis reveals aberrant basaloid cells in restrictive allograft syndrome (RAS) lungs. a) Uniform manifold approximation and projection (UMAP) of 40 390 epithelial single nuclei from 15 RAS, and nine control (CTRL) donor lungs, labelled by cell type (upper UMAP), disease (bottom left), and subject (bottom right) where each colour depicts a distinct subject. b) Boxplots representing the percentage makeup distributions of each epithelial cell type among all identified epithelial cells organised by disease group. Whiskers represent 1.5× interquartile range. Aberrant basaloid cells are significantly increased ($p<0.001$) in RAS compared to control lungs. Detailed results of unadjusted Wilcoxon rank sum test comparing RAS and control proportions are reported in supplementary table E2h. c) Stacked bar plots representing the frequency of each epithelial cell type among all identified epithelial cells per subject. Each bar represents a different subject (15 RAS and nine control subjects). Stacked bars are ordered by increasing frequencies of aberrant basaloid cells. d) Heat map representing characteristics of the six identified epithelial cell types. Expression values are centred and scaled across subjects. Each column shows the average expression per subject and disease state. Each subject is represented by a unique colour, and disease state and epithelial cell type are represented in the coloured annotation bars above. ***: $p<0.001$.

https://doi.org/10.1183/13993003.00537-2025

Downloaded from https://publications.ersnet.org on October 29, 2026 by guest. Please see licensing information on first page for reuse rights.

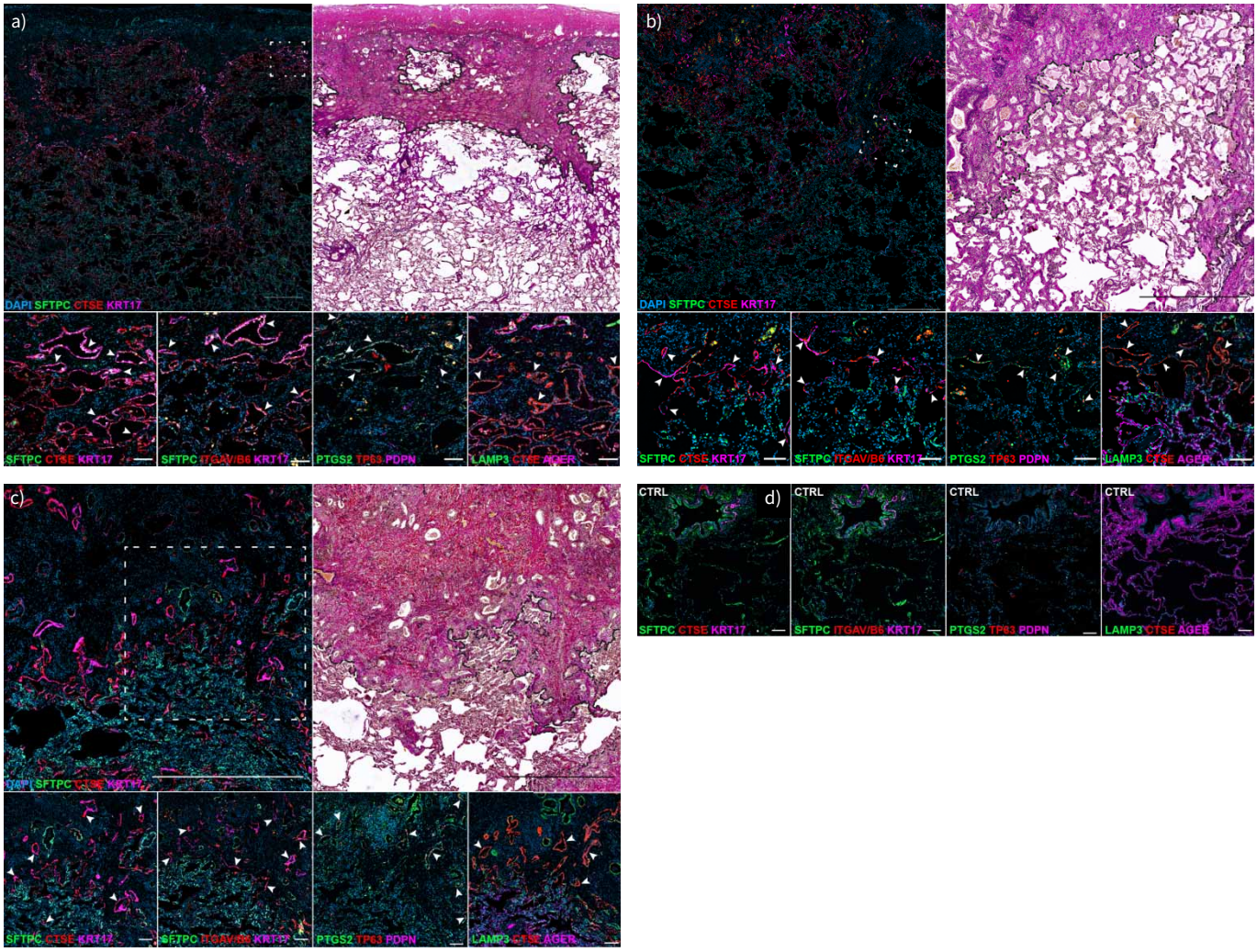


FIGURE 3 Immunofluorescent validation reveals aberrant basaloid cells localised at the fibrotic edge. Immunofluorescent and corresponding Elastica van Gieson (EvG) stains of three different restrictive allograft syndrome (RAS) specimens. Split channels are depicted in supplementary figures E2–E7. Stains of control (CTRL) lungs are depicted in supplementary figures E8–E11. a–c) Overviews (top rows of a–c) scale bars=1000 µm; close-up views (bottom rows of a–c) scale bars=100 µm. Arrows indicate aberrant basaloid cells identified based on the combined staining patterns of *KRT17*, *CTSE*, *integrin αvβ6*, *COX2* and *TP63* within the same microanatomical region (the fibrotic edge) across the respective panels. Immunofluorescent stains demonstrate their preferential localisation at the fibrotic edge and partial expansion into the alveolar space and alveolar fibroelastosis areas. In proximity to the fibrotic edge, multiple "obliterating alveoli" (air-containing structures in fibrotic areas) are observed. They show a heterogeneous cellular composition, typically including aberrant basaloid cells, and variably also *SFTPC*$^{+}$/*KRT17*$^{+}$ transitional cells and *LAMP*$^{+}$/*AGER*$^{+}$ alveolar type 1 (AT1) cells. In concordance with our transcriptomic data, immunofluorescent stains show no bronchiolisation. EvG stains confirm the alveolar fibroelastosis pattern in RAS. Dashed black lines serve as guides for the identification of the fibrotic edge. d) Immunofluorescent stains of control lungs, showing a bronchiole with *KRT17*$^{+}$/*TP63*$^{+}$ basal cells. Scale bars=100 µm. DAPI: 4′,6-diamidino-2-phenylindol.

E2–E7, E23). Throughout the samples, we observed and quantified an epithelial gradient in RAS: aberrant basaloid cells occur frequently at the fibrotic edge and become increasingly rare toward healthy-looking alveoli, until eventually disappearing (supplementary figure E24a and b). In contrast to IPF, myofibroblast foci covered by aberrant basaloid cells were a rare histological finding in RAS. No aberrant basaloid cells were detected in control specimens (supplementary figures E8–E11).

Fully developed AFE is characterised by a homogeneous, pauci-cellular fibrosis with preserved elastic fibres of the remnant alveolar walls, which are denuded of epithelial cells, while the former alveoli are filled with collagen. Near the fibrotic edge, we consistently observed multiple air-containing structures,

Downloaded from https://publications.ersnet.org on October 29, 2026 by guest. Please see licensing information on first page for reuse rights.

which we termed "obliterating alveoli". Lining epithelial cells of obliterating alveoli have lost contact to remnant alveolar walls due to thick collagen depositions (EvG stains in figure 3). Obliterating alveoli consist of aberrant basaloid cells, *SFTPC*$^+$/*KRT17*$^+$ transitional cells, and *LAMP*$^+$/*AGER*$^+$ AT1 cells, most of which are pathologically *CTSE*$^+$ (figure 3, supplementary figure E24d–f). Although combinations of these cell types exist, most obliterating alveoli contain at least some aberrant basaloid cells (supplementary figure E24d–f). In general, aberrant basaloid cells seem to exclusively appear in monolayers, regardless of their localisation in RAS lung tissue.

The endothelial cell repertoire is shifted towards ectopic COL15A1$^+$ *peribronchial vascular endothelial cells, and shows a loss of* PRX$^+$ *alveolar microvasculature*

27 657 single nuclei (n=15 309 RAS; n=12 348 control), representing 26.1% of all profiled nuclei, were identified as endothelial cells (ECs) based on distinct markers (figure 4a–d, supplementary table E2d). We identified all known EC populations of the human lung in all specimens, including arterial endothelial cells, aerocytes, general capillary endothelial cells (gCAPs), venous endothelial cells, lymphatic endothelial cells, and *COL15A1*$^+$ pVECs (figure 4a–d, supplementary table E2d) [26]. *COL15A1*$^+$ pVECs are known to form vessels adjacent to major airways and subpleural vessels, and their transcriptomic profile (*e.g. COL15A1*, *PLVAP*, *SPRY1*, *ZNF385D*) aligned with previous studies (figure 4d, supplementary table E2d) [17, 26]. Pathway analysis suggests unique signalling through *e.g.* insulin receptor, calcitonin-like ligands and tachykinin receptors (supplementary figure E26). In RAS, the endothelial repertoire showed a significant increase in *COL15A1*$^+$ pVECs (1.9% *versus* 8.2%, unadjusted p=0.04, Wilcoxon rank-sum test) (figure 4b, supplementary table E2h). Additionally, we observed a nonsignificant trend toward a decreased fraction of aerocytes in RAS (median percentage 11.2% RAS *versus* 26.0% control, unadjusted p=0.055) (figure 4b).

Immunofluorescence revealed ectopic COL15A1$^+$ *pVECs in RAS, partially replacing* PRX$^+$ *alveolar microvasculature*

We validated the presence of *COL15A1*$^+$ pVECs using antibodies against their distinctive markers *COL15A1* and *PLVAP* alongside the pan-endothelial marker *CD31*. In control specimens, *COL15A1*$^+$ pVECs are strictly limited to peribronchial vasculature or to larger vessels of the pleura and do not contribute to the normal alveolar microvasculature (aerocytes and gCAPs), which stains positive for the pan-microvasculature marker *PRX* (supplementary figures E15–E17) [26]. In RAS, *COL15A1*$^+$ pVECs show a deviating distribution pattern: they are no longer restricted to peribronchial vasculature and pleura, but expand substantially (figure 5, supplementary figure E24c). We refer to all *COL15A1*$^+$ pVECs outside locations adjacent to major airways or the pleura as "ectopic pVECs". This designation is based solely on their spatial localisation, as transcriptomic profiles of ectopic and non-ectopic *COL15A1*$^+$ pVECs were not distinguishable in our study. Remarkably, ectopic pVECs gradually expand parallel to the aberrant basaloid cell gradient, forming vessels at fibrotic areas adjacent to the fibrotic edge. Toward the dense fibrotic subpleural space, we observed a nonsignificant rarefication of ectopic pVECs. However, while ectopic pVECs are extensively present in fibrotic areas, we observed a significantly reduced number of *PRX*$^+$ vessels in these areas compared to the alveolar tissue (figure 5a–c, supplementary figure E24c). Similar to our epithelial findings, ectopic pVECs are not restricted to fibrotic areas, but invade alveolar tissue (figure 5a–c, supplementary figure E24c). Where ectopic pVECs reach into alveolar tissue, we observed a loss of physiological *PRX*$^+$ alveolar microvasculature in both, immunofluorescencce and EvG-IHC stains (figure 5a–f, supplementary figures E12–E14).

Micro-CT imaging with three-dimensional reconstruction revealed pronounced vascular remodelling in the dense zone of subpleural fibrotic consolidation in RAS tissue (figure 5g). Virtual sectioning showed extensive sprouting of vasculature-like structures within the subpleural fibrosis, extending into AFE areas. Most of these vasculature-like structures were *CD31*$^+$ and *COL15A1*$^+$in sequential EvG-IHC stains (figure 5d–f). Morphologically, these vascular structures appear to originate from the pleura, as cross-sections became narrower with increasing distance from the pleura (figure 5g).

The stromal cell compartment contains CTHRC1$^+$ *fibrotic fibroblasts in RAS*

37 905 single nuclei (n=20 712 RAS; n=17 193 control), representing 35.8% of all profiled nuclei, were identified as stromal cells based on distinct markers. They include pericytes, smooth muscle cells (SMC), mesothelium, and fibroblast populations. Within fibroblasts, we identified distinct subpopulations, including alveolar fibroblasts, stressed alveolar fibroblasts, adventitial fibroblasts, and *CTHRC1*$^+$ fibrotic fibroblasts (figure 6a–d, supplementary table E2e) [27]. While *CTHRC1*$^+$ fibrotic fibroblasts were found in RAS and control subjects, they compose a significantly higher fraction of all stromal cells in RAS compared to controls (median percentage among stromal cells: 21.5% RAS *versus* 6.4% control, p=0.0002) (figure 6b, supplementary table E2h). In contrast, the fraction of alveolar fibroblasts in RAS is

Downloaded from https://publications.ersnet.org on October 29, 2026 by guest. Please see licensing information on first page for reuse rights.

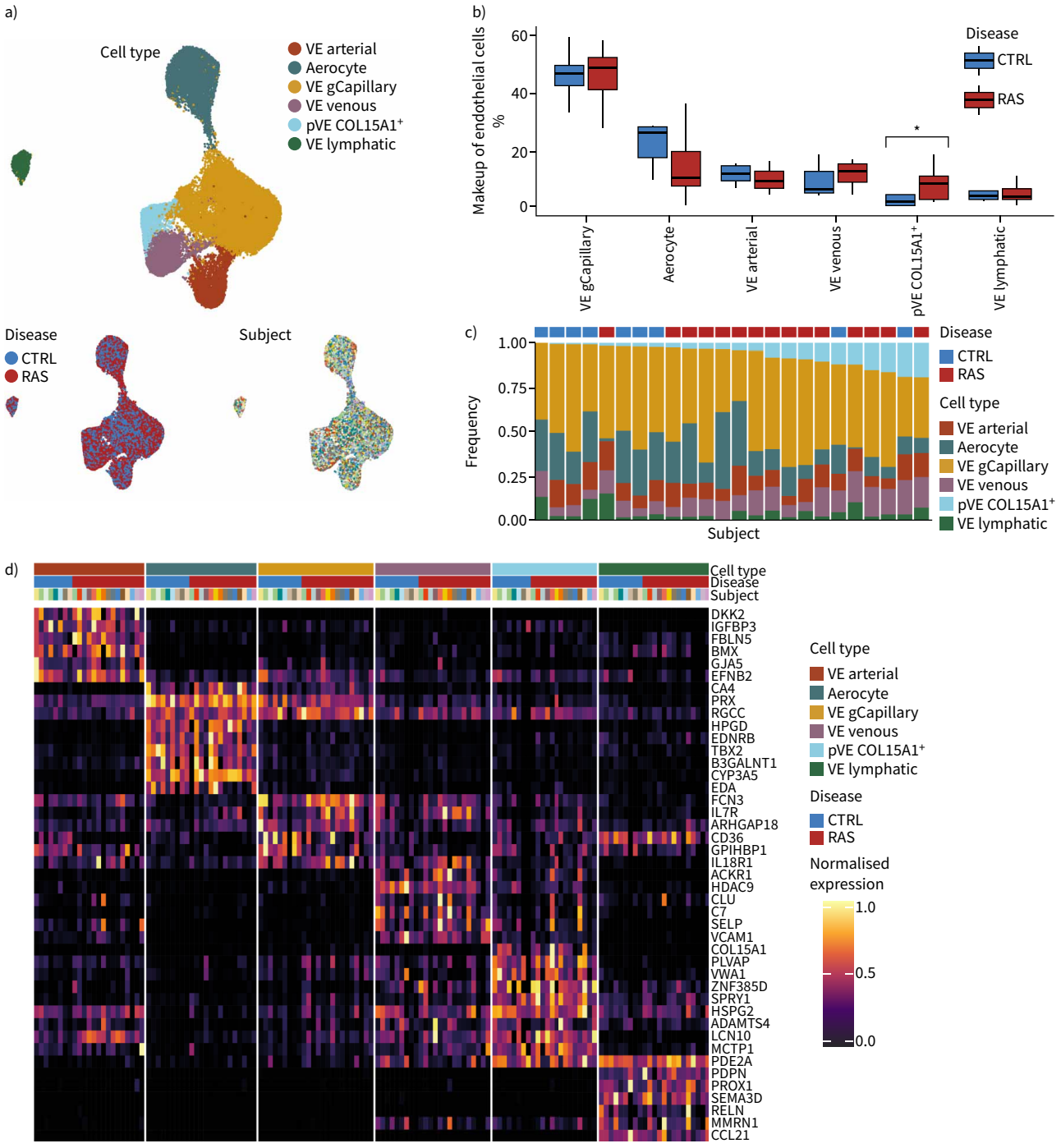


FIGURE 4 Identification of increased *COL15A1*$^{+}$ peribronchial vascular endothelial cells (pVECs) in restrictive allograft syndrome (RAS). a) Uniform manifold approximation and projection (UMAP) of 27 657 endothelial single nuclei from 15 RAS, and nine control (CTRL) donor lungs, labelled by cell type (upper UMAP), disease (bottom left), and subject (bottom right) where each colour depicts a distinct subject. b) Boxplots representing the percentage distributions of each endothelial cell type among all identified endothelial cells organised by disease group. Whiskers represent 1.5× interquartile range. *: p<0.05. COL15A1^{+} pVECs are significantly increased (p<0.05) in RAS compared to control lungs. Detailed results of unadjusted Wilcoxon rank sum test comparing RAS and control proportions are reported in supplementary table E2h. c) Stacked bar plots representing the frequency (in %) of each endothelial cell type among all identified endothelial cells per subject. Each bar represents a different subject (15 RAS and nine control subjects). Stacked bars are ordered by increasing frequencies of *COL15A1*$^{+}$ pVECs. d) Heat map representing marker gene expression of the six identified endothelial cell types. Gene expression is unity normalised between 0 and 1 across endothelial cells. Each column shows individual cell average marker gene expression per subject and disease state. Each subject is represented by a unique colour, and disease state and endothelial cell type are represented in the coloured annotation bars above.

Downloaded from https://publications.ersnet.org on October 29, 2026 by guest. Please see licensing information on first page for reuse rights.

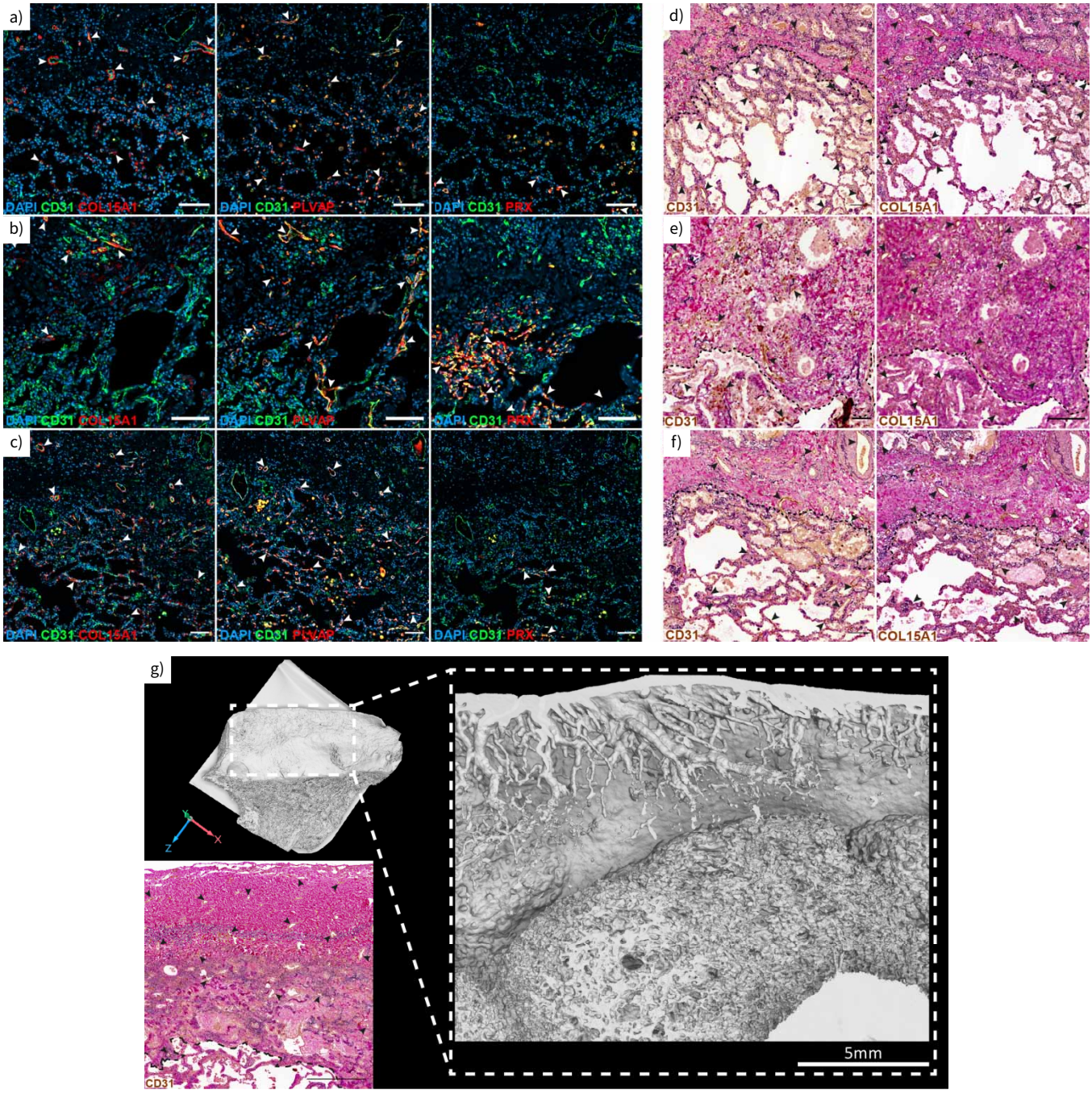


FIGURE 5 Localisation of *COL15A1*$^+$ peribronchial vascular endothelial cells in restrictive allograft syndrome (RAS). a–c) Immunofluorescent stains of three different RAS specimens. Split channels are depicted in supplementary figures E12–E14. Stains of control (CTRL) lungs are depicted in supplementary figures E15–E17. Arrows in *CD31/COL15A1* and *CD31/PLVAP* panels indicate *CD31*$^+$*/COL15A1*$^+$*/PLVAP*$^+$ (ectopic) peribronchial vascular endothelial cells (pVECs). pVECs occur in high frequencies in alveolar fibroelastosis (AFE) areas. They also expand into the alveoli, where they partially replace the physiological *CD31*$^+$*/PRX*$^+$ microvasculature (arrows in *CD31/PRX* panels indicate physiological alveolar capillaries). d–f) Elastica van Gieson (EvG) immunohistochemistry (IHC) stains of RAS specimens corresponding to the Immunofluorescent stains in a–c). Arrows indicate *CD31*$^+$ VECs and *COL15A1*$^+$ ectopic pVECs. Positive staining aligns with the observations made in a–c). EvG-IHC staining show that ectopic pVECs in AFE regions lack spatial connections to former alveolar septa or other physiological structures, suggesting a neoangiogenic potential. Dashed black lines serve as guides for the identification of the fibrotic edge. Scale bars=100 µm, unless otherwise stated. g) Micro-computed tomography (CT) imaging of subpleural RAS remodelling. Three-dimensional reconstruction of the tissue specimen shows a dense zone of subpleural fibrotic consolidation. Tungsten contrasting does not contrast fibrotic tissue. Virtual sectioning of the block indicates pronounced sprouting of vasculature-like structures within the subpleural fibrosis. Morphologically, vascular structures seem to originate from the pleura, as cross-sections of the observed vessels rejuvenate with increasing distance from the pleura. EvG-IHC staining of a RAS specimen. Scale bar=500 µm. Arrows indicate *CD31*$^+$ VECs, confirming vascular-like structures seen in micro-CT scans as vessels. The combination with *COL15A1* targeted IHC-EvG stains reveals that these vessels are mostly (ectopic) pVECs.

Downloaded from https://publications.ersnet.org on October 29, 2026 by guest. Please see licensing information on first page for reuse rights.

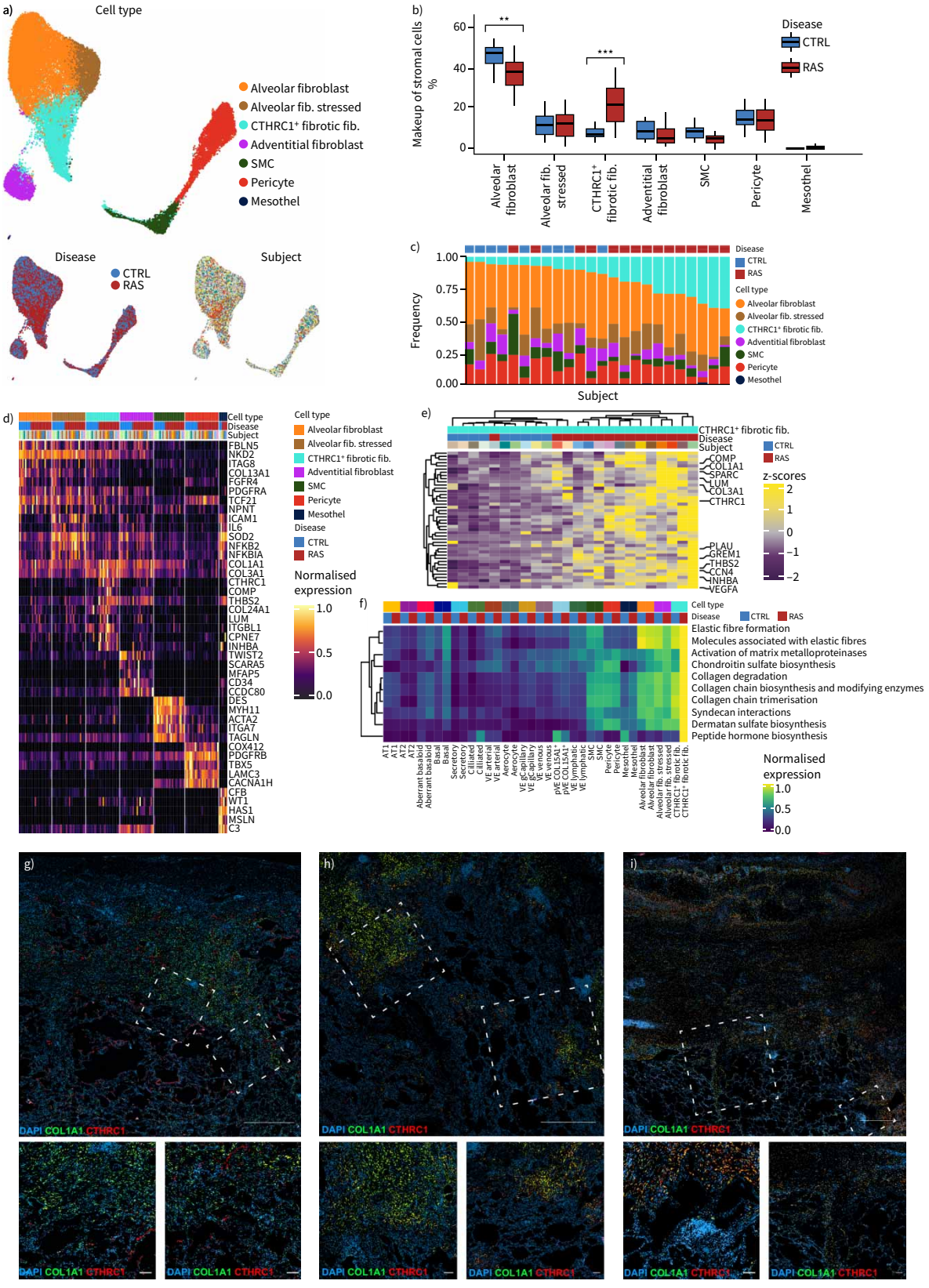


FIGURE 6 Identification and localisation of *CTHRC1*$^{+}$ fibrotic fibroblasts (fib.) in restrictive allograft syndrome (RAS). a) Uniform manifold approximation and projection (UMAP) of 37 905 stromal single nuclei from 15 RAS, and nine control (CTRL) donor lungs, labelled by cell type (upper UMAP), disease (bottom left), and subject (bottom right) where each colour depicts a distinct subject. b) Boxplots representing the nonzero-percent makeup distributions of each stromal cell type among all identified stromal cells organised by disease group. Whiskers represent

Downloaded from https://publications.ersnet.org on October 29, 2026 by guest. Please see licensing information on first page for reuse rights.

1.5× interquartile range. RAS and control cell type frequencies were compared using the Wilcoxon rank sum test (detailed results are presented in supplementary table E2h). Alveolar fibroblasts are significantly decreased (unadjusted p<0.01) in RAS compared to control lungs and *CTHRC1*$^+$ fibrotic fibroblasts are significantly increased (unadjusted p<0.001) in RAS compared to control lungs. c) Stacked bar plots representing the frequency (in %) of each stromal cell type among all identified stromal cells per subject. Each bar represents a different subject (15 RAS and nine control subjects). Stacked bars are ordered by increasing frequencies of *CTHRC1*$^+$ fibrotic fibroblasts. d) Heat map representing the marker gene expression of the seven identified stromal cell types. Gene expression is unity normalised between 0 and 1 across stromal cells. Each column shows average gene expression per subject and disease state. Each subject is represented by a unique colour, and disease state and stromal cell type are represented in the coloured annotation bars above. e) Heat map of differentially expressed genes comparing RAS and controls in *CTHRC1*$^+$ fibrotic fibroblasts, hierarchically clustered. Average expression values are scaled across subjects. Each subject is represented by a unique colour, and disease state and cell type are represented in the coloured annotation bars above. f) Pathway analysis of 15 RAS and nine control specimens. Depicted are average enrichment scores per cell type and disease state. Enrichment scores are unity normalised between 0 and 1 across all identified cell types. Cell type and disease status are indicated by the coloured annotation bars above. g–i) RNA *in situ* hybridisation (RNA-ISH) staining of three different RAS specimens. Scale bar of overviews (top row)=1000 µm; scale bars of close-up views (bottom row)=100 µm. Split channels are depicted in supplementary figures E18–E20. Stains of control lungs are depicted in supplementary figure E21. *CTHRC1*$^+$*/COL1A1*$^+$ cells represent *CTHRC1*$^+$ fibrotic fibroblasts which are distributed across all parts of alveolar fibroelastosis areas and form small nests in fibrotically thickened alveolar septa. SMC: smooth muscle cell; mesothel: mesothelium; AT1: alveolar type 1; VE: vascular endothelial cell type. **: p<0.01, ***: p<0.001.

significantly reduced (RAS *versus* control: 38.0% *versus* 48.5%, unadjusted p=0.005) (figure 6b). The identified *CTHRC1*$^+$ fibrotic fibroblasts exhibited a distinct transcriptional profile: aside from *CTHRC1*, they exhibit the highest expression of collagens *COL1A1* and *COL3A1*, extracellular matrix-related genes such as *COMP*, *LUM*, *SPARC*, *THBS2*, *POSTN*, *FN1*, the growth factor *VEGFA*, the matricellular protein *CCN4*, the TGF-β signalling pathway activator *INHBA*, and the secreted serine protease *PLAU* (figure 6d and e, supplementary table E2e). Biological pathways enriched in *CTHRC1*$^+$ fibrotic fibroblasts include elastic fibre formation; chondroitin sulfate, dermatan sulfate and peptide hormone biosynthesis; activation of matrix metalloproteinases; collagen degradation, collagen chain biosynthesis and modifying enzymes, and collagen chain trimerisation (figure 6f, supplementary table E2f). Taken together, marker gene expression and enriched pathways of *CTHRC1*$^+$ fibrotic fibroblasts highlight their prominent role in the fibrotic remodelling of AFE.

RNA-ISH reveals localisation of CTHRC1$^+$ *fibrotic fibroblasts in RAS*

RNA-ISH stains of *CTHRC1*$^+$*/COL1A1*$^+$ fibrotic fibroblasts revealed a predominant localisation of *CTHRC1*$^+$ fibrotic fibroblasts in areas of AFE in RAS, with only very few *CTHRC1*$^+$ fibrotic fibroblasts observed in controls (supplementary figure E21). *CTHRC1*$^+$ fibrotic fibroblasts are ubiquitously distributed across all areas of AFE, occasionally forming fibroblast foci at the fibrotic edge. In contrast to aberrant basaloid and ectopic pVECs, *CTHRC1*$^+$ fibrotic fibroblasts were present in all areas of fibrosis, not only at the fibrotic edge. Outside fibrotic AFE areas, *CTHRC1*$^+$ fibrotic fibroblasts were sporadically observed in small nests in thickened alveolar septa in more distal RAS tissue, but not in healthy-looking alveolar walls (figure 6g–i, supplementary figures E18–E20, and E24g–h).

Discussion

In this study, we provide the first single-cell transcriptomic catalogue of structural lung cells in human RAS. Our snRNA-seq data revealed aberrant basaloid cells, *COL15A1*$^+$ pVECs and *CTHRC1*$^+$ fibrotic fibroblasts overlapping with previously identified cell populations in IPF [17]. Other IPF-associated changes, such as proximalisation of the alveolar epithelium, where AT1 and AT2 cells are replaced by airway cell populations, were not observed, since our data show neither a significant decline in AT1 and AT2 cells, nor an increase in airway-derived cells (figure 2b) [17]. We validated the previously unknown presence of aberrant basaloid cells, ectopic *COL15A1*$^+$ pVECs and *CTHRC1*$^+$ fibroblasts in RAS by IHC, immunofluorescence and RNA-ISH, and identified their unique distribution patterns.

While allograft airway epithelial cells have been linked to fibroproliferation and aberrant tissue repair in BOS [28, 29], little was known about epithelial changes in RAS. Aberrant basaloid cells are disease-associated cells, which have been found in IPF and scleroderma with pulmonary involvement, and to a much lesser extent in COPD [17, 20, 21]. Their origin remains elusive, but recent research indicates that human AT2 cells can transdifferentiate into aberrant basaloid cells [30]. Their discovery in the human RAS lung suggests previously unknown commonalities between these clinically distinct entities, as their expression profile closely matches the aberrant basaloid cell population identified by Adams *et al*. [17] in human IPF lungs. Our data indicate a relevant contribution of this cell population to the pathogenesis and/or disease progression of RAS for the following reasons: first, we identified aberrant basaloid cells in all but one of our RAS specimens, but none in control specimens, supporting the hypothesis that aberrant

Downloaded from https://publications.ersnet.org on October 29, 2026 by guest. Please see licensing information on first page for reuse rights.

basaloid cells are a pathognomonic feature of fibrotic lung diseases in general and a hallmark of RAS specifically. Second, their unique expression profile may promote the fibrotic remodelling seen in AFE regions of RAS lungs. This is indicated by the EMT-like phenotype, and the high expression of genes associated with the pathogenesis of IPF such as *integrin αVβ6*, *MMP7*, *GDF15* and *EPHB2*. Third, cellular senescence is associated with disease progression in age-related and chronic diseases like IPF, as well as frailty and transplant-specific complications in solid-organ transplants [31]. Thus, aberrant basaloid cells probably drive pathological cellular senescence in RAS due to their expression of multiple senescence markers, including *CDKN1A*, *CDKN2B*, *MDM2* and *GDF15*.

Little is known about the endothelial cell compartment in RAS patients and its possible pathological impacts. Similar to IPF, we observed significantly expanded *COL15A1*$^{+}$*/PLVAP*$^{+}$ ectopic pVECs in RAS, with largely overlapping transcriptomic profiles [17]. In RAS, ectopic pVECs at the fibrovascular interface are characteristically distributed parallel-running to the aberrant basaloid cell gradient, potentially due to repetitive endothelial injury [32]. EvG-IHC staining demonstrated that ectopic pVECs in obliterated AFE regions lack spatial connections to former alveolar septa, indicating potential neoangiogensis. Moreover, wherever ectopic pVECs infiltrate the alveolar microvasculature, normal *PRX*$^{+}$ alveolar capillaries are missing. Similar observations in IPF and nonspecific interstitial pneumonia [17, 30, 33] suggest a contribution of VECs, particularly *COL15A1*$^{+}$ pVECs, to the pathogenesis of RAS and other fibrotic diseases. We hypothesise that these ectopic *COL15A1*$^{+}$*/PLVAP*$^{+}$ pVECs may not possess full barrier function: *PLVAP* forms the diaphragms of fenestrated endothelium, potentially influencing vascular permeability and leukocyte trafficking/transmigration, and is typically absent in mature barrier endothelium [34, 35]. Based on this, we propose that ectopic pVECs might contribute to impaired gas exchange and vascular permeability in the RAS lung. Nonetheless, the origin and exact role of ectopic pVECs in RAS remain enigmatic.

AFE is characterised by collagen-rich fibrosis and hyperelastosis within the remodelled alveolar walls [9, 11, 36–38]. In our data, *CTHRC1*$^{+}$ fibrotic fibroblasts emerged as key mediators of fibroelastotic remodelling in RAS [13, 14], as they express numerous fibrosis-associated genes, including *BMP1*, *COL1A2*, *COL3A1*, *CXCL12*, *CTHRC1*, *MMP2*, *MMP14*, *PLOD2*, *SERPINE1*, *TIMP1* and *TIMP2* [27]. The transcriptional profile of these CTHRC1^{+} fibrotic fibroblasts is highly consistent with that of the *CTHRC1*$^{+}$ myofibroblast subpopulation previously described in IPF [17, 27]. Pathway analysis in *CTHRC1*$^{+}$ fibrotic fibroblasts revealed key pathomechanisms of AFE, including elastogenesis, collagenesis, elastic fibre and extracellular matrix formation, organisation, and regulation. The fibroblast to *CTHRC1*$^{+}$ myofibroblast conversion through *SFRP1*$^{+}$ transitional fibroblasts has been recently unravelled [39]. *CTHRC1*$^{+}$ fibrotic fibroblasts are known key drivers of fibrosis, not only in the lung (*e.g.* IPF and scleroderma-associated interstitial lung disease), but in organ fibrosis throughout [40–42].

While our data reveal multiple unexpected similarities between IPF and RAS, it is equally important to emphasise their differences: in IPF, aberrant basaloid cells characteristically line the active edge of pathognomonic myofibroblast foci [17], whereas myofibroblast foci are rare in RAS. Further, the histo-anatomical distribution of ectopic pVECs differs between IPF and RAS: in IPF, ectopic pVECs are associated with areas of bronchiolisation, whereas in RAS, bronchiolisation is absent, and ectopic pVECs primarily localise in AFE areas, possibly contributing to a shift from pulmonary to systemic perfusion.

Currently, no effective therapy for RAS is available. In this context, our observation of markedly elevated expression levels of genes encoding the integrin subunits αvβ6 in aberrant basaloid cells is of potential relevance. Integrin αvβ6 can activate latent TGF-β1, and its high expression is known to substantially contribute to organ fibrosis [43]. Integrin αvβ6 therefore emerged as a promising therapeutic target for IPF [44]. Moreover, increased expression levels of TGF-β1 have also been reported in bronchoalveolar lavage analysis from RAS patients and linked to the development of BOS [45, 46]. Collectively, these observations raise the possibility that integrin αvβ6 may also play a role in RAS pathogenesis and could represent a candidate target for future therapeutic investigations. Our snRNA-seq dataset may serve as a reference atlas for exploring the relevance and applicability of antifibrotic strategies in RAS.

Our study has certain limitations. First, the size of our cohort may not capture the complete heterogeneity of RAS. However, we analysed samples from 15 well-characterised RAS patients, which represents a substantial number given the rarity of this condition. Due to limited availability of suitable specimens, the same cohort had to be used for both transcriptomic profiling and histological validation. Second, analysing end-stage RAS tissue provides insights into the pathophysiological characteristics of RAS, which may be more ambiguous or absent in earlier disease stages. Furthermore, this single-time-point study could not study mechanisms of disease progression. Third, due to the integration approach of our snRNA-seq data analysis, some nuclei of our control specimens were spuriously identified as aberrant basaloid cells and as

Downloaded from https://publications.ersnet.org on October 29, 2026 by guest. Please see licensing information on first page for reuse rights.

CTHRC1$^+$ fibrotic fibroblasts. However, their gene expression profiles showed substantially reduced expression of major aberrant basaloid/*CTHRC1*$^+$ fibrotic fibroblast-specific marker genes (figures 2d and 6d and e, supplementary figure E26C). Fourth, as we provide nuclei data, capturing the entire transcriptome is inherently not possible, but we still cover the large majority of transcripts at a single-cell resolution. Furthermore, given the limited availability of published snRNA-seq data in IPF profiled with the same technology, we restricted our comparisons to IPF to qualitative alignments based on shared marker genes and cell-type identities. Future single-cell or single-nucleus RNA-seq datasets will be needed to confirm and complement our findings. Fifth, as histological protein marker expression was evaluated using serial tissue sections, definitive multitarget co-expression at the single-cell level cannot be determined; interpretations therefore rely on concordant localisation across adjacent microanatomical regions. And last, to enable a focused and high-resolution analysis, we concentrated on RAS and the structural cell compartment. A simultaneous characterisation of immune cell populations or a comparative

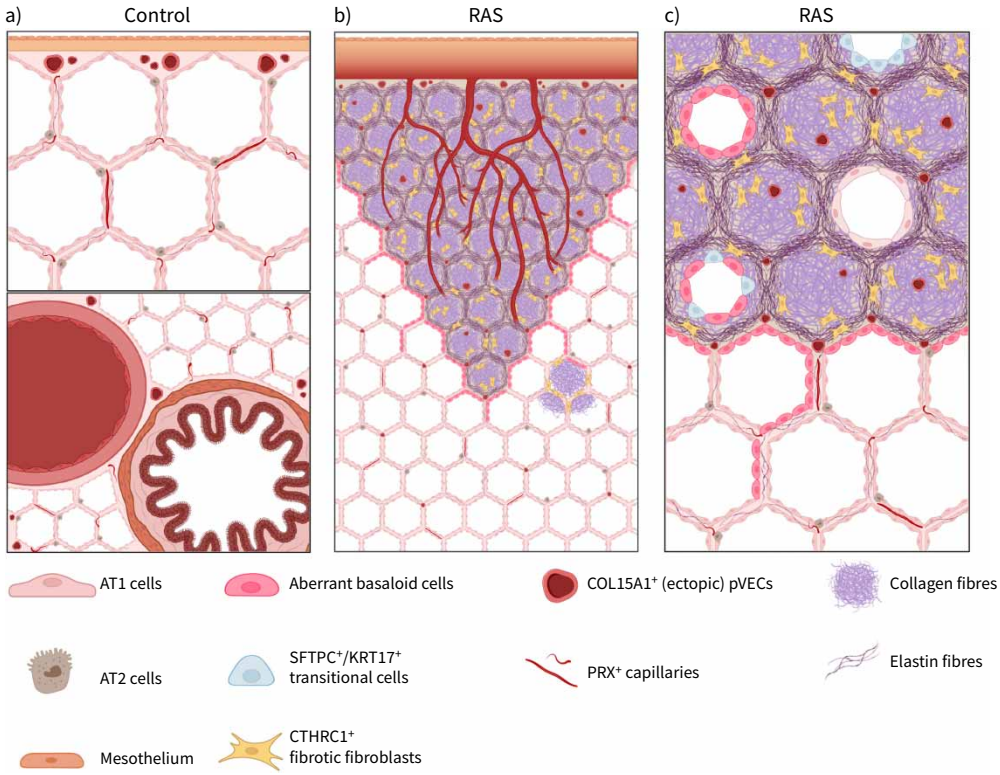


FIGURE 7 Graphical summary of aberrant and ectopic cells in restrictive allograft syndrome (RAS). a) Schematic illustration of healthy lung tissue. The upper illustration shows the mesothelial coated pleura, and subpleural lung tissue including *COL15A1*$^+$ vessels near the pleura, alveoli, elastin fibres in alveolar septa, alveolar type 1 (AT1) and AT2 cells, and *PRX*$^+$ capillaries. The lower illustration shows healthy lung tissue including a bronchus and its corresponding bronchial artery, peribronchial *COL15A1*$^+$ vessels, alveoli, elastin fibres in alveolar septa, AT1 and AT2 cells, and *PRX*$^+$ capillaries. b) Schematic overview illustration of RAS lung tissue. It shows characteristic elements of RAS such as a thickened pleura, areas of alveolar fibroelastosis (AFE), vasculature-like structures within the subpleural fibrosis reaching into AFE areas and rejuvenating with increasing distance from the pleura, *COL15A1*$^+$ vessels near the pleura and ectopic *COL15A1*$^+$ vessels in areas of AFE and in alveolar septa where they partially replace *PRX*$^+$ capillaries, a decreased amount of *PRX*$^+$ capillaries, *CTHRC1*$^+$ fibrotic fibroblasts in areas of AFE and sporadically in small nests in thickened alveolar septa in more distal RAS tissue, aberrant basaloid cells lining the active edge of the fibrotic edge in a monolayer and lining thickened alveolar septa, and enriched elastic fibres in thickened alveolar septa. c) Schematic close-up illustration of RAS lung tissue. It shows characteristic elements of RAS such as AFE, ectopic *COL15A1*$^+$ vessels in areas of AFE and in alveolar septa where they partially replace *PRX*$^+$ capillaries, a decreased amount of *PRX*$^+$ capillaries, *CTHRC1*$^+$ fibrotic fibroblasts in areas of AFE, aberrant basaloid cells lining the active edge of the fibrotic edge in a monolayer and lining thickened alveolar septa, obliterating alveoli near the fibrotic edge consisting of either aberrant basaloid cells, *SFTPC*$^+$/*KRT17*$^+$ transitional cells, and *LAMP*$^+$/*AGER*$^+$ AT1 cells, all of which being pathologically *CTSE*$^+$, and enriched elastic fibres in thickened alveolar septa. pVEC: peribronchial vascular endothelial cell.

Downloaded from https://publications.ersnet.org on October 29, 2026 by guest. Please see licensing information on first page for reuse rights.

transcriptomic analysis including BOS would have required the integration of extensive additional datasets. Given the limited existing knowledge on RAS, such breadth was not feasible within a single study and should therefore be addressed in future investigations.

Taken together, this study, in combination with previous scRNA-seq studies in fibrotic lung diseases [17, 20, 21], reveals a striking but common cellular similarity in fibrotic lung diseases, despite differing histomorphological patterns, such as the usual interstitial pneumonia pattern in IPF and AFE pattern in RAS. Specifically, we observed that the fibrotic niche in both diseases is consistently formed by aberrant basaloid cells, ectopic *COL15A1*$^{+}$ pVECs, and *CTHRC1*$^{+}$ fibrotic fibroblasts (figure 7a–c). These findings provide a strong rationale for further investigating the potential transferability of IPF-specific therapeutic strategies to RAS. The unexpected transcriptomic similarity of key fibrotic cell populations in both diseases suggests overlapping molecular mechanisms that may be therapeutically exploitable. Nonetheless, future studies are needed to validate these parallels and assess their translational relevance.

Acknowledgements: We are indebted with great gratitude to all patients who enabled conducting this study by their participation. We thank the Fiedler lab, the Braun lab, and the Prasse lab for the generous provision of their lab devices, and Regina Engelhardt (Institute of Pathology, Hannover Medical School, Hannover, Germany) for excellent histopathological support. Figures 1a, 7 and the graphical abstract were created using BioRender.com.

Ethics statement: All biological materials and data were collected following written informed consent from the patients and approval from the ethics committee of Hanover Medical School (IRB number 10141_BO_K_2022).

Author contributions: J.C. Schupp conceptualised, acquired funding, and supervised the study. J. Gottlieb performed cohort characterisation and phenotyping. L. Neubert, F. Laenger, D.D. Jonigk, F. Ius, J. Salman, J.C. Kamp and M. Kühnel procured, processed, and characterised RAS and control specimens. L.M. Leiber and L. Christian dissociated the lungs and isolated the nuclei. M. Ballmaier performed FANS. L.M. Leiber, L. Christian and J.C. Schupp performed snRNA-seq barcoding and library construction. L.M. Leiber, L. Christian and the Research Core Unit Genomics (RCUG) of MHH conducted quality control of the libraries. B. Haermeyer and A.K. Bergmann performed sequencing. All sequencing data were processed, curated, visualised and analysed by J.C. Schupp and L.M. Leiber. HE, IHC and IF including quantification were performed by L.M. Leiber and J. Ruwisch, and analysed by L.M. Leiber, J.C. Schupp, J. Ruwisch, L. Neubert and D.D. Jonigk. Histology images were generated by L.M. Leiber. L. Christian prepared the samples for micro-CT experiments, which were scanned by J. Ruwisch and L. Knudsen, and analysed by J. Ruwisch, L. Knudsen, J.C. Schupp and L.M. Leiber. E.K.J. Schwarz created the graphical abstracts based on specifications from J.C. Schupp and L.M. Leiber. M. Greer, A. Justet, U. Martin, A.Ö. Yildirim, B.M. Vanaudenaerde, R. Vos, J.M. Hohlfeld, H. Beeckmans, C. Falk and N. Kaminski provided critical interpretation, review, and commentary on data and the manuscript. The manuscript was drafted by L.M. Leiber and J.C. Schupp and reviewed and edited by all authors.

Conflicts of interest: L.M. Leiber reports a grant from Department of Pneumology at Hannover Medical School. J. Ruwisch reports grants from PRACTIS-Program of Hannover Medical School for Clinician Scientists (Deutsche Forschungsgemeinsschaft/DZL), and payment or honoraria for lectures, presentations, manuscript writing or educational events from Boehringer Ingelheim. J.C. Kamp reports grants from the Else Kröner Fresenius Foundation (EKFS) and the German Research Foundation (DFG). M. Greer reports payment or honoraria for lectures, presentations, manuscript writing or educational events from Therakos (UK), and participation on a data safety monitoring board or advisory board with ECLAD (UK) Study. C. Werlein payment or honoraria for lectures, presentations, manuscript writing or educational events from Boehringer Ingelheim. A. Justet reports grants from ANR – MLQ-CT and Fondation du Souffle, and support for attending meetings from Sanofi. R. Vos reports grants from the Research Foundation Flanders (FWO). B.M. Vanaudenaerde reports grants from KU Leuven. F. Ius reports grants, consultancy fees and payment or honoraria for lectures, presentations, manuscript writing or educational events from Biotest AG, and support for attending meetings from Biotest AG, Xvivo and Abbott. C. Falk reports support for the present study from Deutsche Krebshilfe, DZL German Center for Lung Diseases Area and DZIF German Center for Infection Research TTU-IICH, payment or honoraria for lectures, presentations, manuscript writing or educational events from Biotest, BioNTech, Amedes, Moderna and Novartis, and support for attending meetings from Biotest. N. Kaminski reports grants from Boehringer Ingelheim, Three Lakes Foundation and BMS, consultancy fees from Boehringer Ingelheim, Pliant, GSK, Merck, Pliant, Three Lake Partners, AstraZeneca, RohBar, Veracyte, CSL Behring, Gilead, Galapagos, Chiesi, Arrowhead, Fibrogen, Sofinnova and Thyro, support for attending meetings from MiRagen and AstraZeneca, stock (or stock options) with Pliant and Thyron, and other financial or non-financial interests with Thyron. J. Gottlieb grants from Deutsche Forschungsgemeinschaft, German Center of Lung Research (DZL) and Zambon, consultancy fees from Sanofi, Moderna, Zambon and Ella CS, payment or honoraria for lectures, presentations, manuscript writing or educational events from Boehringer, Takeda and

Downloaded from https://publications.ersnet.org on October 29, 2026 by guest. Please see licensing information on first page for reuse rights.

AstraZeneca, payment for expert testimony from Allogenetics, participation on a data safety monitoring board or advisory board with the ScanCLAD Trial, and a leadership role with the European Reference Network (ERN) for rare lung diseases. J.C. Schupp reports support for the present study from Else Kröner-Fresenius Foundation, Ministry of Science and Culture of Lower Saxony and German Center for Lung Research, grants from the Ann Theodore Foundation, the German Research Foundation and the Fritz-Thyssen-Foundation, payment or honoraria for lectures, presentations, manuscript writing or educational events from Boehringer, Merck/MSD, GSK, AOP, Boehringer, Kinevant and the Ann Theodore Foundation, support for attending meetings from Boehringer, and patents planned, issued or pending EP-3964214-A1 and US12036218B2. The remaining authors have no potential conflicts of interest to disclose.

Support statement: Supported by Else Kröner-Fresenius Foundation (EKFS, 2023_EKCS.18, 2021_EKEA.16, 2020_EKSP.78), CORE100Pilot Advanced Clinician Scientist Program of Hannover Medical School funded by EKFS and the Ministry of Science and Culture of Lower Saxony, and by German Center for Lung research (FKZ 82DZL002B1, FKZ 82DZL002C1 and FKZ 82DZLT82C1, all to J.C. Schupp), R01HL127349, R01HL141852, U01HL145567, R21HL161723, P01HL11450, and a grant from Veracyte (N. Kaminski), and the Three Lakes Foundation (N. Kaminski). Funding information for this article has been deposited with the Open Funder Registry.

References

1 de Silva T, Voisey J, Hopkins P, *et al.* Markers of rejection of a lung allograft: state of the art. *Biomark Med* 2022; 16: 483–498.
2 Sato M, Waddell TK, Wagnetz U, *et al.* Restrictive allograft syndrome (RAS): a novel form of chronic lung allograft dysfunction. *J Heart Lung Transplant* 2011; 30: 735–742.
3 Smirnova NF, Riemondy K, Bueno M, *et al.* Single-cell transcriptome mapping identifies a local, innate B cell population driving chronic rejection after lung transplantation. *JCI Insight* 2022; 7: e156648.
4 Pakhale SS, Hadjiliadis D, Howell DN, *et al.* Upper lobe fibrosis: a novel manifestation of chronic allograft dysfunction in lung transplantation. *J Heart Lung Transplant* 2005; 24: 1260–1268.
5 Todd JL, Jain R, Pavlisko EN, *et al.* Impact of forced vital capacity loss on survival after the onset of chronic lung allograft dysfunction. *Am J Respir Crit Care Med* 2014; 189: 159–166.
6 Glanville AR, Verleden GM, Todd JL, *et al.* Chronic lung allograft dysfunction: definition and update of restrictive allograft syndrome – a consensus report from the Pulmonary Council of the ISHLT. *J Heart Lung Transplant* 2019; 38: 483–492.
7 Klouda T, Vargas SO, Midyat L. Restrictive allograft syndrome after lung transplantation. *Pediatr Transplant* 2021; 25: e14000.
8 Fernandez IE, Heinzelmann K, Verleden S, *et al.* Characteristic patterns in the fibrotic lung. Comparing idiopathic pulmonary fibrosis with chronic lung allograft dysfunction. *Ann Am Thorac Soc* 2015; 12: Suppl. 1, S34–S41.
9 Jonigk D, Rath B, Borchert P, *et al.* Comparative analysis of morphological and molecular motifs in bronchiolitis obliterans and alveolar fibroelastosis after lung and stem cell transplantation. *J Pathol Clin Res* 2016; 3: 17–28.
10 Verleden SE, Von der Thüsen J, Roux A, *et al.* When tissue is the issue: a histological review of chronic lung allograft dysfunction. *Am J Transplant* 2020; 20: 2644–2651.
11 Ofek E, Sato M, Saito T, *et al.* Restrictive allograft syndrome post lung transplantation is characterized by pleuroparenchymal fibroelastosis. *Mod Pathol* 2013; 26: 350–356.
12 Verleden GM, Glanville AR, Lease ED, *et al.* Chronic lung allograft dysfunction: definition, diagnostic criteria, and approaches to treatment – a consensus report from the Pulmonary Council of the ISHLT. *J Heart Lung Transplant* 2019; 38: 493–503.
13 Lynch TJ, Ahlers BA, Swatek AM, *et al.* Ferret lung transplantation models differential lymphoid aggregate morphology between restrictive and obstructive forms of chronic lung allograft dysfunction. *Transplantation* 2022; 106: 1974–1989.
14 Todd JL, Weigt SS, Neely ML, *et al.* Prognosis and risks for probable chronic lung allograft dysfunction: a prospective multicenter study. *Am J Respir Crit Care Med* 2025; 211: 239–247.
15 Duong A, Moshkelgosha S, Wong AK, *et al.* Single-cell RNA sequencing identifies unique pulmonary macrophage subsets associated with chronic lung allograft dysfunction. *J Heart Lung Transplant* 2022; 41: S20.
16 Leiber LM, Christian L, Neubert L, *et al.* Single-nuclei RNA-seq reveals aberrant cell populations in restrictive allograft syndrome after lung transplantation. *Eur Respir J* 2024; 64: Suppl. 68, OA985.
17 Adams TS, Schupp JC, Poli S, *et al.* Single-cell RNA-seq reveals ectopic and aberrant lung-resident cell populations in idiopathic pulmonary fibrosis. *Sci Adv* 2020; 6: eaba1983.
18 Bankhead P, Loughrey MB, Fernández JA, *et al*. QuPath: open source software for digital pathology image analysis. *Sci Rep* 2017; 7: 16878.

Downloaded from https://publications.ersnet.org on October 29, 2026 by guest. Please see licensing information on first page for reuse rights.

19 Schmidt U, Weigert M, Broaddus C, *et al.* Cell detection with star-convex polygons. *In:* Frangi A, Schnabel J, Davatzikos C, *et al.*, eds. Medical Image Computing and Computer Assisted Intervention - MICCAI 2018. MICCAI 2018. Lecture Notes in Computer Science, vol. 11071. Cham, Springer International Publishing, 2018; pp. 265–273.
20 Habermann AC, Gutierrez AJ, Bui LT, *et al.* Single-cell RNA sequencing reveals profibrotic roles of distinct epithelial and mesenchymal lineages in pulmonary fibrosis. *Sci Adv* 2020; 6: eaba1972.
21 Valenzi E, Tabib T, Papazoglou A, *et al.* Disparate interferon signaling and shared aberrant basaloid cells in single-cell profiling of idiopathic pulmonary fibrosis and systemic sclerosis-associated interstitial lung disease. *Front Immunol* 2021; 12: 595811.
22 Mayr CH, Santacruz D, Jarosch S, *et al.* Spatial transcriptomic characterization of pathologic niches in IPF. *Sci Adv* 2024; 10: eadl5473.
23 Svobodová B, Löfdahl A, Kadefors M, *et al.* Collagen VII is associated with airway remodeling, honeycombing, and fibroblast foci in usual interstitial pneumonia/idiopathic pulmonary fibrosis. *Am J Pathol* 2025; 195: 1467–1483.
24 Uthaya Kumar DB, Motakis E, Yurieva M, *et al.* Bronchial epithelium epithelial-mesenchymal plasticity forms aberrant basaloid-like cells *in vitro*. *Am J Physiol Lung Cell Mol Physiol* 2022; 322: L822–L841.
25 Wu B, Shichino S, Ueha S, *et al. Ex vivo* lung-organoid model for aberrant basaloid cell induction and activation. *Inflamm Regen* 2025; 45: 33.
26 Schupp JC, Adams TS, Cosme C, *et al.* Integrated single-cell atlas of endothelial cells of the human lung. *Circulation* 2021; 144: 286–302.
27 Tsukui T, Sun KH, Wetter JB, *et al.* Collagen-producing lung cell atlas identifies multiple subsets with distinct localization and relevance to fibrosis. *Nat Commun* 2020; 11: 1920.
28 Belperio JA, Weigt SS, Fishbein MC, *et al.* Chronic lung allograft rejection: mechanisms and therapy. *Proc Am Thorac Soc* 2009; 6: 108–121.
29 Estenne M, Hertz MI. Bronchiolitis obliterans after human lung transplantation. *Am J Respir Crit Care Med* 2002; 166: 440–444.
30 Lang NJ, Gote-Schniering J, Porras-Gonzalez D, *et al. Ex vivo* tissue perturbations coupled to single-cell RNA-seq reveal multilineage cell circuit dynamics in human lung fibrogenesis. *Sci Transl Med* 2023; 15: eadh0908.
31 Lorenz EC, Hickson LJ, Khairallah P, *et al.* Cellular senescence and frailty in transplantation. *Curr Transplant Rep* 2023; 10: 51–59.
32 Ackermann M, Werlein C, Plucinski E, *et al.* The role of vasculature and angiogenesis in respiratory diseases. *Angiogenesis* 2024; 27: 293–310.
33 Schupp JC, Manning EP, Chioccioli M, *et al.* Alveolar vascular remodeling in nonspecific interstitial pneumonia: replacement of normal lung capillaries with *COL15A1*-positive endothelial cells. *Am J Respir Crit Care Med* 2023; 208: 819–822.
34 Denzer L, Muranyi W, Schroten H, *et al.* The role of PLVAP in endothelial cells. *Cell Tissue Res* 2023; 392: 393–412.
35 van der Wijk A, Wisniewska-Kruk J, Vogels IMC, *et al.* Expression patterns of endothelial permeability pathways in the development of the blood-retinal barrier in mice. *FASEB J* 2019; 33: 5320–5333.
36 Piper PJ, Vane JR, Wyllie JH. Inactivation of prostaglandins by the lungs. *Nature* 1970; 225: 600–604.
37 Montero MA, Osadolor T, Khiroya R, *et al.* Restrictive allograft syndrome and idiopathic pleuroparenchymal fibroelastosis: do they really have the same histology? *Histopathology* 2017; 70: 1107–1113.
38 Braubach P, Werlein C, Verleden SE, *et al.* Pulmonary fibroelastotic remodelling revisited. *Cells* 2021; 10: 1362.
39 Mayr CH, Sengupta A, Asgharpour S, *et al.* Sfrp1 inhibits lung fibroblast invasion during transition to injury-induced myofibroblasts. *Eur Respir J* 2024; 63: 2301326.
40 Valenzi E, Bulik M, Tabib T, *et al.* Single-cell analysis reveals fibroblast heterogeneity and myofibroblasts in systemic sclerosis-associated interstitial lung disease. *Ann Rheum Dis* 2019; 78: 1379–1387.
41 Ruiz-Villalba A, Romero JP, Hernández SC, *et al.* Single-cell RNA-seq analysis reveals a crucial role for CTHRC1 (Collagen Triple Helix Repeat Containing 1) cardiac fibroblasts after myocardial infarction. *Circulation* 2020; 142: 1831–1847.
42 Gur C, Wang SY, Sheban F, *et al.* LGR5 expressing skin fibroblasts define a major cellular hub perturbed in scleroderma. *Cell* 2022; 185: 1373–1388.
43 Sheppard D. Integrin-mediated activation of latent transforming growth factor β. *Cancer Metastasis Rev* 2005; 24: 395–402.
44 Lancaster L, Cottin V, Ramaswamy M, *et al.* Bexotegrast in patients with idiopathic pulmonary fibrosis: the INTEGRIS-IPF clinical trial. *Am J Respir Crit Care Med* 2024; 210: 424–434.
45 Sacreas A, von der Thüsen JH, van den Bosch TPP, *et al.* The pleural mesothelium and transforming growth factor-β_1 pathways in restrictive allograft syndrome: a pre-clinical investigation. *J Heart Lung Transplant* 2019; 38: 570–579.
46 Morrone C, Smirnova NF, Jeridi A, *et al.* Cathepsin B promotes collagen biosynthesis, which drives bronchiolitis obliterans syndrome. *Eur Respir J* 2021; 57: 2001416.

Downloaded from https://publications.ersnet.org on October 29, 2026 by guest. Please see licensing information on first page for reuse rights.